JOURNAL OF AIRCRAFT
Vol. 45, No. 5, September–October 2008

Numerical Analysis on Flight-Test Results of Supersonic Experimental Airplane NEXST-1

Hiroaki Ishikawa*
Sankosoft Company, Ltd., Shinjuku, Tokyo 169-0075, Japan
and
Dong-Youn Kwak† and Kenji Yoshida‡
Japan Aerospace Exploration Agency, Mitaka, Tokyo 181-0015, Japan

DOI: 10.2514/1.33595

A flight test of a supersonic experimental airplane (National Experimental Supersonic Transport, NEXST-1) was successfully conducted by the Japan Aerospace Exploration Agency in October of 2005. The experimental airplane was designed to reduce drag on supersonic cruise condition by means of some conventional and advanced design concepts: arrow wing planform, warp wing, area-ruled body, and natural laminar flow wing. The purpose of this study was to make clear the verification of those design concepts on the experimental airplane using the computational fluid dynamics analysis. The computational fluid dynamics results were compared with the flight-test results. The aeroelastic deformation and boundary layer transition were taken into account in the computational fluid dynamics analysis. This comparison highlighted the quantitative benefit of the natural laminar flow wing design concept. Furthermore, a real size supersonic transport could be designed using the drag reduction design technologies already validated from the NEXST-1 flight test. The results helped clarify the net drag reduction potentially attainable on a full-scale supersonic transport.

Nomenclature

AR	=	wing aspect ratio
C_D	=	drag coefficient
$C_{D\min}$	=	minimum drag coefficient
C_L	=	lift coefficient
C_{L0}	=	C_L at minimum drag on drag-polar curve
$C_{L\alpha}$	=	lift slope
C_m	=	pitching moment coefficient
C_{m0}	=	C_m at $\alpha = 0$
$C_{m\alpha}$	=	pitching moment slope
C_p	=	pressure coefficient
c	=	chord length, m
H	=	altitude, km
K	=	coefficient of drag-polar curve
L/D	=	lift-to-drag ratio
M	=	Mach number
Re	=	Reynolds number based on the mean aerodynamic chord length
T_{Lo}	=	time from the liftoff of the NEXST-1
α	=	angle of attack
α_0	=	angle of attack at $C_L = 0$

I. Introduction

A FLIGHT test of the supersonic experimental airplane (National Experimental Supersonic Transport: NEXST-1) [1] was conducted successfully by the Japan Aerospace Exploration Agency (JAXA) in October of 2005 at Woomera test range in Australia [2]. A lot of aerodynamic data were obtained from the flight test [3] to validate the aerodynamic design technology [4]. As shown in Fig. 1, the four design concepts, arrow wing planform, warp wing, area-ruled body, and natural laminar flow wing, were applied to the NEXST-1 to improve aerodynamic performance at supersonic cruise condition (lift coefficient $C_L = 0.1$ and Mach number $M = 2.0$).

The arrow wing planform with an optimum slenderness ratio was selected from the supersonic linear theory [5] in compromising aerodynamics and structural constraints. The wing aspect ratio is 2.2 and the swept angle of the leading edge is 66 deg (inner wing) and 61.2 deg (outer wing), which are subsonic leading edges at $M = 2.0$. To reduce the lift-dependent drag, a warped wing was designed by using Carlson's method [6]. The optimum load distribution can be obtained by the optimum combination of the wing camber and twist distributions. A supersonic area-ruled body was also applied to reduce the wave drag due to volume. The fuselage was designed so that the cross-sectional area distribution of overall shape of the aircraft is the same as that of the equivalent Sears-Haack body [7]. The natural laminar flow wing design concept is based on suppressing the Tollmien–Schlichting wave instability and the crossflow instability. To suppress both instabilities, we found an optimum pressure distribution using a practical transition prediction method based on the e^N method [8]. This pressure distribution had a sharply increased pressure gradient at the narrow region of the front part of the wing and had gradual pressure gradients at other chord locations. Then the natural laminar flow wing was designed from the above pressure distribution using an inverse design method and a computational fluid dynamics (CFD) analysis. Then we designed the NEXST-1 airplane, which is a scale ratio of 11% of the real supersonic transport (SST) aircraft and is 11.5 m in length.

In this study, the four aerodynamic design concepts [9] were verified by comparing the flight-test results with a CFD analysis. When the CFD results were compared to the flight-test results, the following two effects were considered to the CFD analysis to improve the accuracy of the CFD: 1) the static aeroelastic deformation, and 2) the boundary layer transition of the wing upper surface. Furthermore, a large scale SST was designed using the aerodynamic design concepts that were verified from the above research using the NEXST-1 flight-test results.

Presented as Paper 3925 at the 25th AIAA Applied Aerodynamics Conference, Miami, Florida, 25–28 June 2007; received 30 July 2007; revision received 1 November 2007; accepted for publication 4 November 2007.

*Researcher, Supersonic Transport Team, Aviation Program Group; hiroaki@chofu.jaxa.jp. Member AIAA.

†Senior Researcher, Supersonic Transport Team, Aviation Program Group; kwak.dongyoun@jaxa.jp. Member AIAA.

‡Section Leader, Supersonic Transport Team, Aviation Program Group; yoshida.kenji@jaxa.jp. Member AIAA.

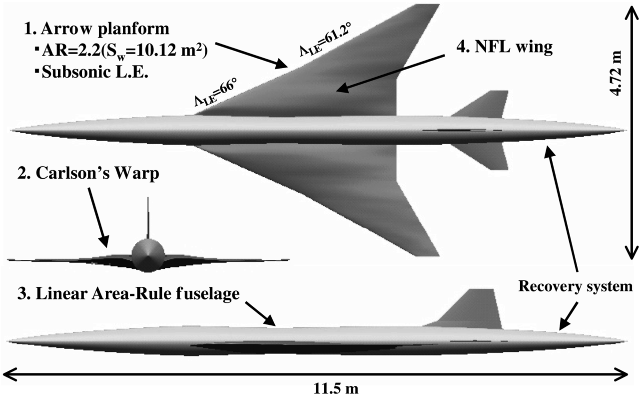

Fig. 1 Schematics of the supersonic experimental airplane (NEXST-1).

II. CFD Validation

A. CFD Codes

In this study, two kinds of CFD codes, the structured mesh code (unified platform for aerospace computation simulation: UPACS) and the unstructured mesh code (Tohoku University aerodynamic simulation: TAS), were used. The UPACS [10] is the structured mesh code developed by JAXA and is a standard CFD code in the Institute of Aerospace Technology of JAXA. The Navier–Stokes flow solver of UPACS is based on a cell-centered finite volume method. The convection terms are discretized using Roe's flux difference splitting with the monotone upstream-centered schemes for conservation laws (MUSCL) extrapolation and no limiter in the present computation. The matrix-free Gauss–Seidel (MFGS) implicit method is used for time integration.

The TAS [11] code, including the mesh generator and flow solver, was the unstructured mesh code developed by Tohoku University and was improved by JAXA. It can generate a triangular surface mesh with the advancing front method, a tetrahedral volume mesh by the method of Delauny tetrahedral meshing, as well as hybrid volume mesh composed of tetrahedrons, prisms, and pyramids for viscous flow with a high Reynolds number. In the TAS code, Navier–Stokes equations are solved on the unstructured mesh by a cell-vertex finite volume method. The Harten–Lax–van Lee–Einfeld–Wada (HLLEW) method is used for the numerical flux computations. The second-order spatial accuracy is obtained by a linear reconstruction of the primitive variable. The lower/upper symmetric Gauss–Seidel (LUSGS) implicit method is used for the time integration.

The Spalart–Allmaras one equation model [12] is used to simulate turbulent flow in both codes.

B. CFD Validation

The CFD codes were verified using the wind-tunnel test results that were performed in a 1×1 m^2 supersonic wind tunnel at JAXA. The aerodynamic forces and the surface pressure distributions were obtained on an 8.5% scaled model of the NEXST-1 in the wind-tunnel test, as shown in Fig. 2. The wind-tunnel tests were performed on two model configurations. One is a clean shape configuration ("clean shape") of the NEXST-1 composed of the wing, fuselage, and tails. The other is a configuration of the NEXST-1 with some additional parts for the flight test ("additional shape"). And both models have the same configuration for the wings, fuselage, and tails. However, the additional shape has a very complex shape to solve for the CFD analysis using the structured mesh code UPACS. In this study, the clean shape was mainly performed on the comparison of the CFD analysis and the flight-test results, because the effect of the additional parts does not have a large influence on the verification of the CFD analysis. It is given in detail in the next section.

Figure 3 shows the comparison of the force data of the wind-tunnel test with that of the CFD for the clean shape. Included were the disk-type roughnesses on the wind-tunnel test model to make turbulent flow, and the CFD analysis was performed in a fully turbulent flow.

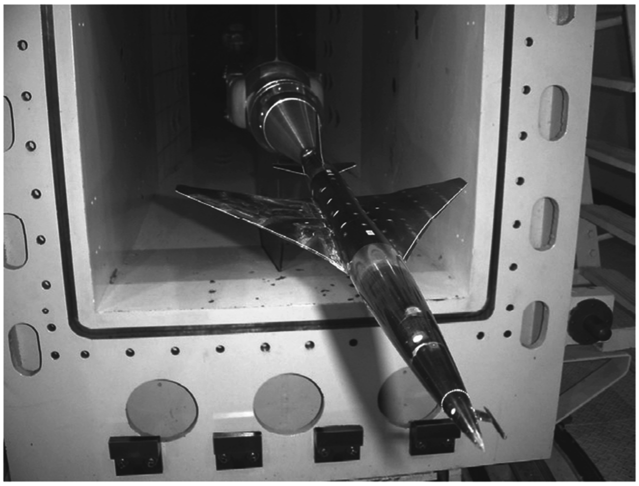

Fig. 2 8.5% scaled model in wind-tunnel test.

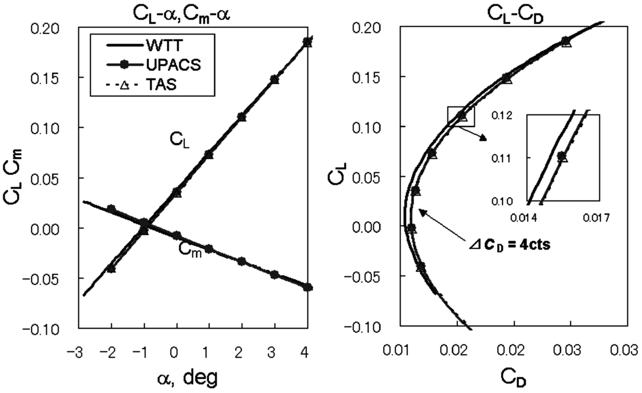

a) $C_L - \alpha$, $C_m - \alpha$ b) $C_L - C_D$

Fig. 3 Comparison of the force data between the wind-tunnel test (WTT) and CFD ($M = 2.0$).

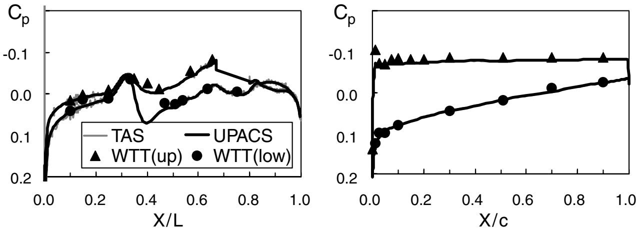

a) y/s=0.0 b) y/s=0.3

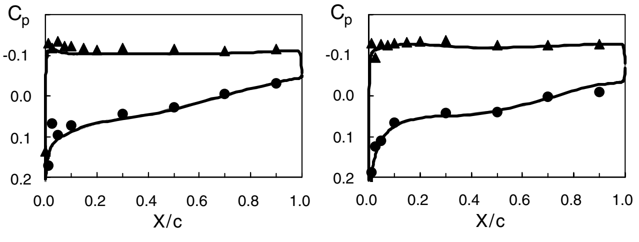

c) y/s=0.5 d) y/s=0.7

Fig. 4 Comparison of C_p distributions between the wind-tunnel test and CFD ($M = 2.0$).

Figure 4 shows the surface C_p distribution on four cross sections of the fuselage and wing by the CFD and the wind-tunnel test. When the CFD results by the UPACS code were compared with the TAS code, good agreement was observed on both results. Further, the CFD results were compared with the wind-tunnel test results. The aerodynamic force by the CFD relatively corresponded with the wind-tunnel tests (Fig. 3). A small difference of $C_{D\min}$ ($\Delta C_{D\min} = 0.0004$: 4 drag counts) was seen in both results. However, the C_p distribution (Fig. 4) by the CFD corresponded to the wind-tunnel test results. By comparing the CFD analysis with the wind-tunnel test, the CFD codes could be verified.

C. Effect of Additional Parts

Before the comparison of the CFD analysis and the flight-test results, it is necessary to estimate the effect of the additional parts. There are two configurations for the CFD analysis of NEXST-1. One is a clean shape configuration (clean shape) of the NEXST-1 composed of the wing, fuselage, and tails. The other is a configuration of the NEXST-1 with some additional parts for the flight test. The additional parts consisted of the following four parts: 1) an air data system (ADS) probe, 2) a total temperature sensor (TAT), 3) a monitor camera with a faring (camera), and 4) a pit joint for the rocket booster (pit joint) (Fig. 5). The CFD analysis was also performed on the two model configurations (clean shape and additional shape). However, the additional shape has a very complex shape to solve for the CFD analysis using the structured mesh code UPACS. Therefore, the CFD analysis using the UPACS was mainly performed on the clean shape. The effects due to the additional parts were estimated using the TAS analysis, because the TAS code using the unstructured mesh can solve the complexity of the additional shape. Thus, the effects by the additional parts were cleared by the wind-tunnel tests and the CFD analysis using the TAS code.

At first, the effect of the additional parts for the aerodynamic forces is investigated. Figure 6 shows the aerodynamic forces obtained by the wind-tunnel test and the CFD analysis. The differences were not observed for the C_L, C_m characteristic on both results. However, the additional parts increased 5.8 counts of the drag component on the wind-tunnel test result. Increments of 5.8 counts of the drag component can be divided into each additional part. 2.0 counts of the C_D increment is induced by the ADS. The TAT increased 2.5 counts of C_D, camera increased 0.7 counts, and the pit joint increased 0.6 counts of the drag component. This fact indicated that the TAT and the ADS had larger effects on the drag coefficient than the others. 8.3 counts of the C_D increment of the additional parts were also estimated by the CFD analysis (TAS). This C_D increment from 5 counts to 8 counts can be considered to be dependent on the pressure drag, because the increment of the surface area of the additional parts is 0.3% of the total area, which corresponds to 0.2 counts of the friction drag increment. Therefore, it suggested that the same effects (increments of 5–8 counts drag components) were induced by the additional parts in the flight tests. When the CFD analysis by the UPACS (clean shape) was compared with the flight-test (additional shape) results, the effect of the additional parts should be considered in the drag component.

Then, the effect of the additional parts for the surface C_p distribution was investigated. At first, the influence of the C_p distributions by only the ADS to the downstream on the wing surface was investigated. Next, the influence of the surface C_p distributions by all of the additional parts was investigated. Figure 7 shows the comparison of C_p distributions on the fuselage and the wing surface of the NEXST-1 with and without the ADS. It was found that the ADS did not affect downstream C_p distributions. Next, the influence of all of the additional parts to the surface C_p distributions was investigated using unstructured CFD results. Figure 8 shows C_p distributions at four cross sections obtained by the CFD analysis and the flight test. Figure 8f shows the surface C_p distribution by the unstructured CFD (TAS) results on the NEXST-1 with the additional parts. With the additional parts, it was observed that the C_p distributions were not changed globally, whereas local changes were observed on the lower wing by the camera and the TAT sensor (Fig. 8). From the above results, it was confirmed that the additional parts were sensitive to drag coefficient C_D, but insensitive to C_L, C_m, and C_p distributions on the wing.

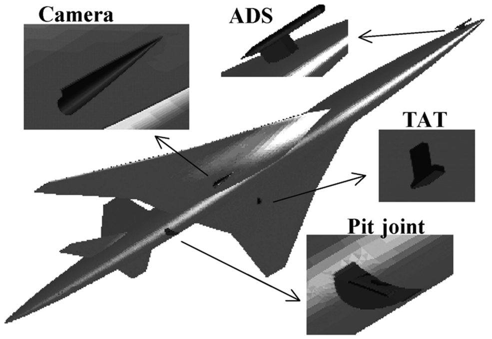

Fig. 5 Configuration of additional parts on the NEXST-1.

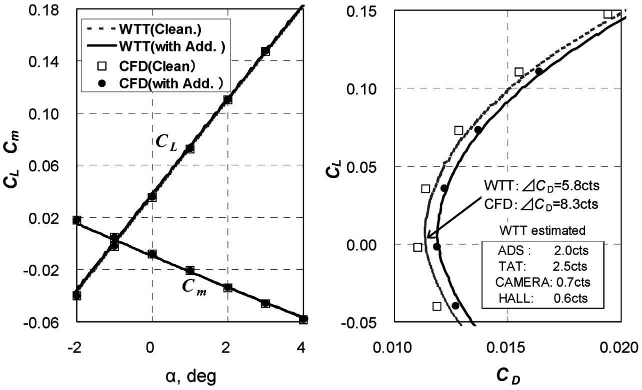

Fig. 6 Effects of the additional parts on the force data ($M = 2.0$).

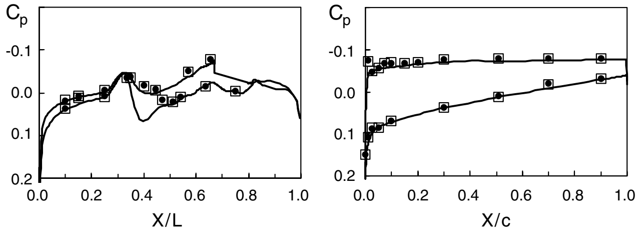

a) y/s=0

b) y/s=0.3

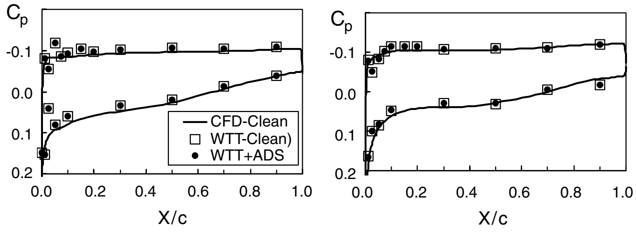

c) y/s=0.5

d) y/s=0.7

Fig. 7 Effects of ADS on C_p distributions ($M = 2.0$).

III. CFD Analysis on Flight-Test Condition

A. Flight Test

Figure 9 shows the flight-test plan for the NEXST-1 program. The experimental airplane was launched using a rocket booster and accelerated to $M = 2.3$ at an altitude of 19 km. The airplane separated from the rocket and started to glide through its aerodynamic measurement phases, hence, the so-called angle of attack sweep, "α sweep," and the Reynolds number sweep, "Re sweep." The Mach number of the measurement phase is around 2. After the measurement phases, the airplane reduced its flight speed and descended and finally touched down using a parachute and air bags. The aerodynamic data were measured, and the experimental airplane was recovered safely. During the flight test, three types of

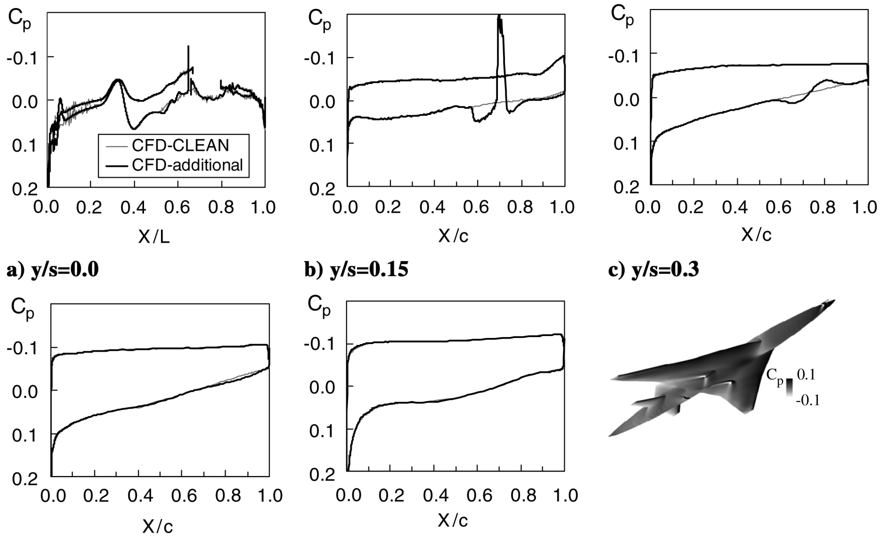

a) y/s=0.0 b) y/s=0.15 c) y/s=0.3

d) y/s=0.5 e) y/s=0.7 f) C_p distribution

Fig. 8 Effects of the additional parts on C_p distributions at the flight condition ($M = 2.0$).

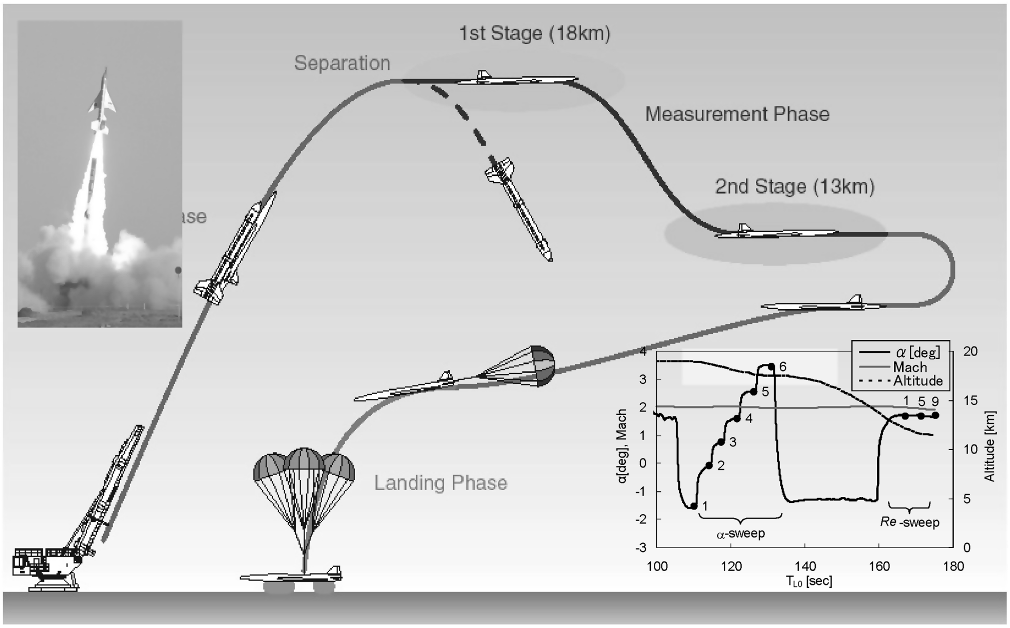

Fig. 9 Flight-test plan of the NEXST-1 program.

aerodynamic data were obtained to validate the design concepts: 1) surface pressure distribution, 2) boundary layer transition, and 3) aerodynamic forces.

The CFD results were compared with the flight-test results to verify the design concepts of the NEXST-1. There were two aerodynamic measurement phases near $H = 18$ km and 12 km at $M = 2.0$ during the flight test. The first one is called an α sweep, and the other one is called a Re sweep. On the α-sweep phase, the angle of attack changes to six steps by pitch and pause. Table 1 shows the flight conditions during each step of the aerodynamic measurement phase. The fourth step of the α sweep is a design point of the NEXST-1. Thus, the CFD analysis was performed on the condition of Table 1. During the measurement phase, the flight speed of the NEXST-1 is kept approximately $M = 2$ by descending the altitude. It is suggested that the force data of the C_L, C_m, and C_D characteristics can be considered by accounting the same Mach number.

B. Improvement of the CFD Analysis

In this section, the flight test and the CFD analysis were compared in detail. Efforts were made to improve the accuracy of the CFD analysis of the flight-test conditions. The first was the effect of aeroelastic deformation of the NEXST-1 airplane during the flight test. The other one was the effect of the boundary layer transition on the wing's upper surface. These effects were very important because they were different from the wind-tunnel test conditions. In this study, the CFD analysis was divided into three types as follows: AS, ES, and TR as shown in Table 2. The AS was performed in a fully turbulent flow with the aerodynamic shape. The aerodynamic shape

Table 1 The CFD analysis conditions

Phase	Altitude, km	Mach	α, deg
α-sweep-1	18.917	2.00	−1.52
α-sweep-1	18.775	2.02	−0.09
α-sweep-2	18.440	2.03	0.77
α-sweep-3	18.039	2.02	1.59
α-sweep-4	17.677	2.00	2.54
α-sweep-6	17.468	1.97	3.45
Re-sweep-5	11.646	1.95	1.68

Table 2 CFD analysis types on the flight-test condition

	Shape	Turbulence
AS	Aerodynamic shape	Fully turbulence
ES	Elastic shape (wing)	Fully turbulence
TR	Elastic shape (wing)	Laminar + turbulence

was designed to improve aerodynamic performance at supersonic cruise conditions ($C_L = 0.1$ and $M = 2.0$). The ES means aeroelastic shape considering the effect of static aeroelastic deformation from the AS using the finite element method (FEM) by NASTRAN. It was also in a fully turbulent flow. And the TR shape is the same as the elastic shape. Further, it was combined in laminar and turbulent flows. The ES shape was obtained from using the span load distribution on the AS shape. Figure 10 shows the wing section geometry of the elastic shapes (ES). As the angle of attack was increased, the dihedral angle, the twist angle, and the camber of the wing changed along the spanwise locations [13]. It was found that the C_p distribution near the wing tip of the ES shape was closer to the flight-test result than the AS shape. The results suggested the necessity for applying aeroelastic deformation to the CFD analysis of the flight-test condition, because the experimental airplane's wing bent more than the wind-tunnel test's. Figure 11 shows the boundary layer transition location obtained from the transition measurement system of the flight test [14,15]. The transition location is specified in the CFD analysis according to the three types of transition measurement sensors: hot-film, dynamic pressure transducer (DPAC), and Preston tube. The line is the boundary of nonturbulent and turbulent regions. Type TR was performed by the CFD analysis considering effects of the boundary layer transition. The upstream region of the transition line is set to the laminar flow and the downstream region is the turbulent flow. The transition location moves more downward at the design point than that of the off-design points. It indicated that the natural laminar flow wing design concept of NEXST-1 was performed successfully at the design points of the flight test. The results also suggested the necessity for applying the effect of the boundary layer transition to the CFD analysis of the flight-test condition, because the transition locations were different at each measurement step.

C. Comparison of CFD with Flight Test

Figures 12 and 13 show the force data of the C_L, C_m, and C_D characteristics of the flight test and the CFD analysis. Figure 14 shows the coefficient of Eqs. (1–3) of C_L, C_m, and C_D which is approximated by the least-squares approximation. This figure is useful to understand the effect of the ES and the TR, where the CFD analysis was performed using the structured CFD code, UPACS, because it has been confirmed the UPACS and the unstructured CFD code, TAS, also have good agreement in the condition of the flight test. Compared with the CFD analysis and the flight test, C_L and C_m of the elastic shape are close to the flight-test result. As Fig. 14 shows, these closing tendencies are observed not only for $C_{L\alpha}$ and $C_{m\alpha}$, but

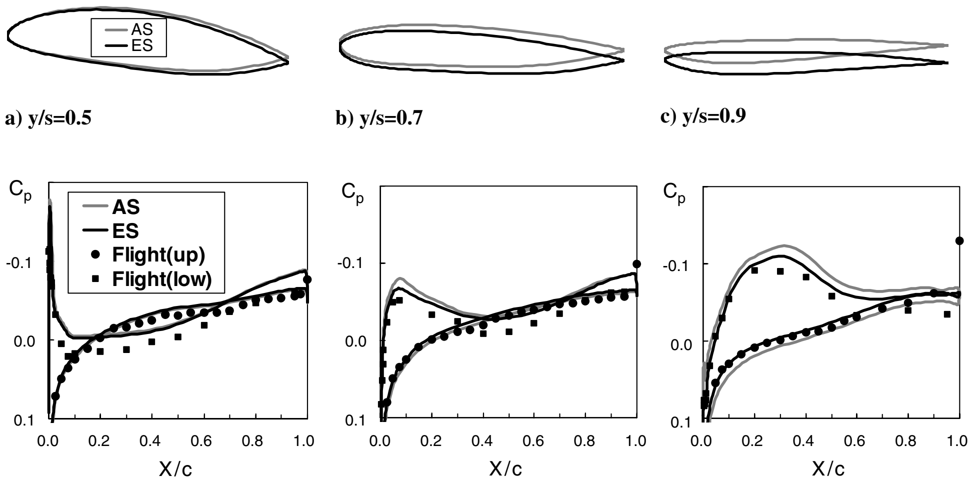

a) y/s=0.5

b) y/s=0.7

c) y/s=0.9

d) C_p, y/s=0.5

e) C_p, y/s=0.7

f) C_p, y/s=0.9

Fig. 10 Comparison of wing cross section and C_p distribution between aeroelastic and aerodynamic shapes.

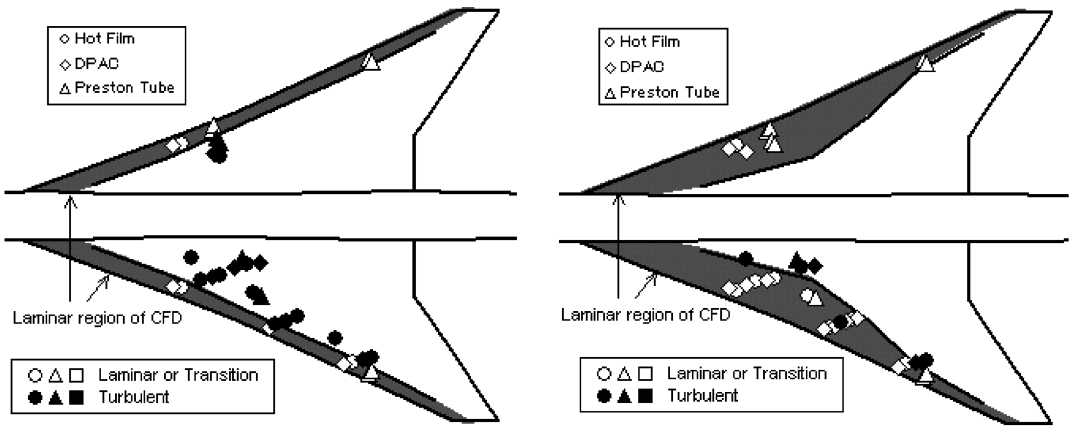

a) Off-design point (α = -0.09deg)

b) Design point (α = 1.59deg)

Fig. 11 Transition location at the design and off-design conditions.

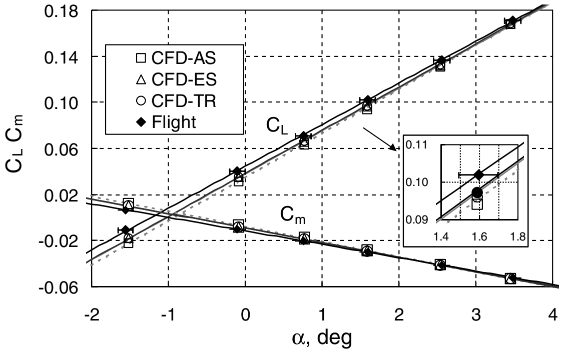

Fig. 12 C_L **and** C_m **characteristics on the** α**-sweep test phase.**

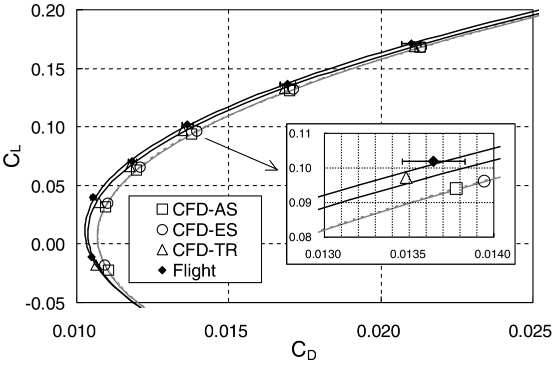

Fig. 13 Drag polar on the α**-sweep test phase.**

also α_0 and C_{m0}. However, the CFD results were a little different with those of the flight test. Figure 13 shows the drag-polar curves. Compared with the CFD and the flight test, the transition case influenced the C_D and the TR results close to the flight test. Although the $C_{D\min}$ of ES is 4.2 counts larger than the flight-test result, the $C_{D\min}$ of TR is only 1.0 counts larger than the flight test. The decrease of the $C_{D\min}$ results from the reduction of the friction drag due to considering the boundary layer transition. Figure 13 indicates that the effect of the boundary layer transition has more influence on its L/D than the effect of static aeroelastic deformation. Here, considering the additional parts, it is estimated that the discrepancy of the $C_{D\min}$ of the CFD analysis and the flight-test result is from 6 to 9 counts. Figure 15 shows the surface C_p at an off-design point and Fig. 16 is at the design point at several spanwise locations. The error bars ($\Delta C_p = 0.0115$) on the C_p distributions are the uncertainty of the pressure measurement system. It was observed that the C_p distributions by the wing tip of ES were close to the flight-test results. The CFD analysis almost corresponded to the flight-test result; however, it was not perfectly corresponding especially at the lower and inner surfaces. This reason has not been well understood, so it calls for further investigation. However, the discrepancy of the CFD from the flight test becomes small at the design point, and good agreement for the CFD with the flight test is obtained except for the inner wing. The C_p distributions of the flight-test results and the CFD analysis at the design point (Fig. 16) had sharply increased pressure gradients at the narrow region of the front part of the wing and gradual pressure gradients at other chord locations. We found that the C_p distributions at the design point (Fig. 16) corresponded to the target C_p distributions of the natural laminar flow wing compared with the off-design point (Fig. 15). It suggested that the natural laminar flow wing design concept was effective at the design point:

$$C_L = C_{L\alpha}[\alpha - \alpha_0] \tag{1}$$

$$C_D = K(C_L - C_{L0})^2 + C_{D\min} \tag{2}$$

$$C_m = C_{m\alpha} - \alpha + C_{m0} \tag{3}$$

From the previous investigations, the effect of the natural laminar flow wing, which is one of the most important design concepts of the NEXST-1, was estimated from the flight test and the CFD analysis. Figure 17 shows C_D at variable angles of attack. The ΔC_D is the difference of C_D between the ES and the TR. When the ΔC_D is small, it is meant that the drag component of the NEXST-1 including the results about the boundary layer transition decreases by the effect of the natural laminar flow wing design concept. It was found that the effect was the highest at the design point (α-sweep 4, $\alpha = 1.59$ deg), and the C_D was 4.6 counts lower than that of the fully turbulent flow. This 4.6-count reduction indicated the effect of the natural laminar flow wing design concept. It was clear that the natural laminar flow wing design concept of the NEXST-1 was effective during the condition of the flight test.

IV. Application for Aerodynamic Design of a Full Scale SST

In this section, a full scale SST (SST-A, Fig. 18a) was designed using the aerodynamic design concepts for drag reduction that already confirmed their benefit from the NEXST-1 flight test. Because there are some constraints for the design of the NEXST-1, for example, the fuselage diameter was increased by 10% to install measurement equipment, and the parachute container for touching down was installed in the body tail. The SST-A does not have these constraints, but some design concepts such as the arrow wing planform, Carlson's warp wing, and the area-ruled body were applied the same as in the NEXST-1. And each design point on the NEXST-1 and the SST-A have different Reynolds number, because the length of the SST-A is about 9 times that of the NEXST-1. As mentioned previously, since considering boundary layer transition influence its L/D, it was needed to redesign the natural laminar flow wing on the large SST that is different from the NEXST-1's Reynolds number condition. First, the C_p distributions of several cross sections on the upper wing of the SST-A were found to achieve a wide laminar flow region. Then the natural laminar flow wing which satisfied these C_p distributions on the upper wing surface was found from the inversed design method.

We tried to clarify the performance of the SST-A by comparing it to a SST-B (Fig. 18b) that was made based on previous design concepts. The "Concorde" is the most famous supersonic commercial transport, but the detail and exact geometrical data of the Concorde were not published. The SST-B was based on the Concorde's shape from published documents [16] and previous design concepts of SST. Thus, the SST-B has an Ogee wing planform, conical camber warp wing, NACA64A series wing section, and a straight body. The SST-B was also assumed to have a capacity of 100 passengers and is 62 m in length, the same as the Concorde. In other words, the SST-B is a hypothetical Concorde model. Table 3 shows the design concepts and Fig. 18 shows each configuration for the CFD analysis.

We also performed a CFD analysis on the SST-A and the SST-B in the fully turbulent flow without engine nacelle. Figure 19 shows the C_L and C_m characteristics in both models. The C_L-α result shows that the $C_{L\alpha}$ on the SST-A is larger than the SST-B and mostly the C_L on the SST-A is larger than the SST-B. By comparing the angle of attack at the design point where C_L is 0.1, the SST-A's C_L is lower than the SST-B's C_L. This result shows that passengers are more comfortable on the lower floor angle. The $C_{m\alpha}$ also shows the SST-A's pitching moment characteristic is better than SST-B's one, because of the effect of the SST-A's stabilizer. Figure 20 shows a drag polar for the SST-A and the SST-B. The drag of the SST-A is lower than the SST-B in all angles of attack. These drag reductions are 18.6 counts at minimum drag and 10.2 counts at the design point ($C_L = 0.1$). This drag reduction is mainly due to the increase of the wing's aspect ratio or applying the area-ruled body, etc. The L/D at the design point rises from 7.8 for the SST-B to 8.5 for the SST-B in spite of a fully turbulent flow. Additionally, it is needed to consider the boundary layer transition for only the SST-A, because the SST-A has a natural laminar flow wing. So we found that SST-A's wing has a 40% laminar flow region on the upper wing surface at the design point

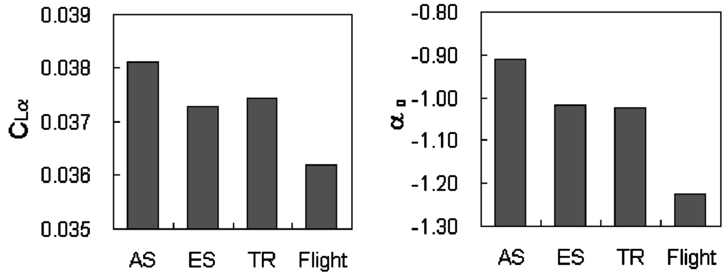

a) Coefficient of fitting C_L

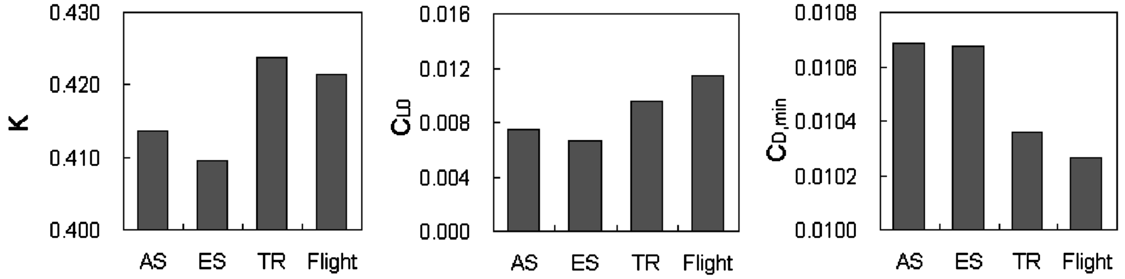

b) Coefficient of fitting C_D

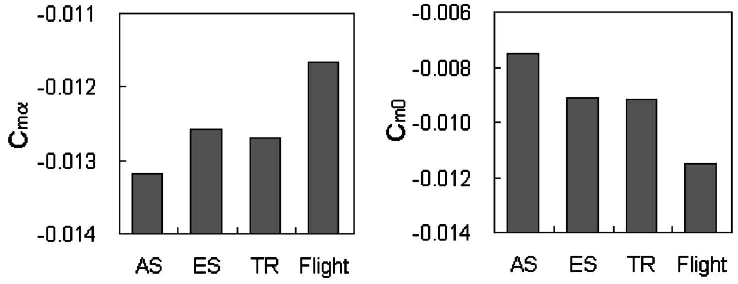

c) Coefficient of fitting C_m

Fig. 14 Coefficient of fitting C_L, C_D, and C_m.

from the boundary layer transition analysis which is based on E to the N method using wing surface C_p distribution by CFD analysis. It calculated that the effect of the natural laminar flow wing of the SST-A has 4.2 counts of drag reduction from the CFD analysis of fully turbulent flow in the same way as the NEXST-1 TR. Finally, we recognized that the L/D of SST-A is an 8.8. This fact shows that the L/D of SST-A progressed by 13% compared with SST-B. Thus, we clarified that the design concepts of the NEXST-1 have better

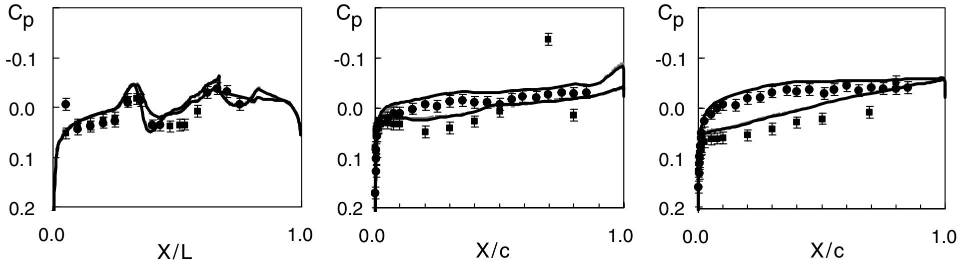

a) y/s=0.0

b) y/s=0.15

c) y/s=0.3

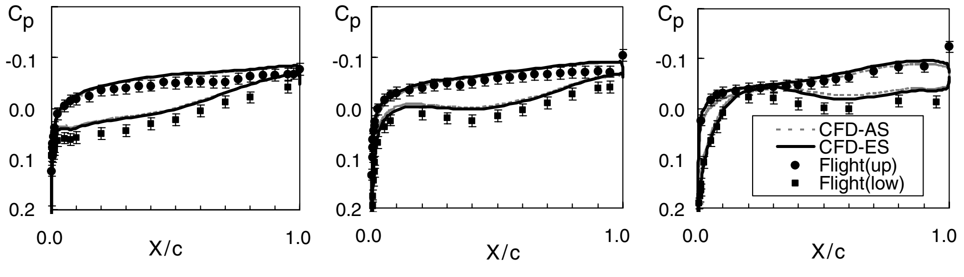

d) y/s=0.5

e) y/s=0.7

f) y/s=0.9

Fig. 15 C_p distribution at the off-design point (α-sweep no. 2, $\alpha = -0.09$ deg).

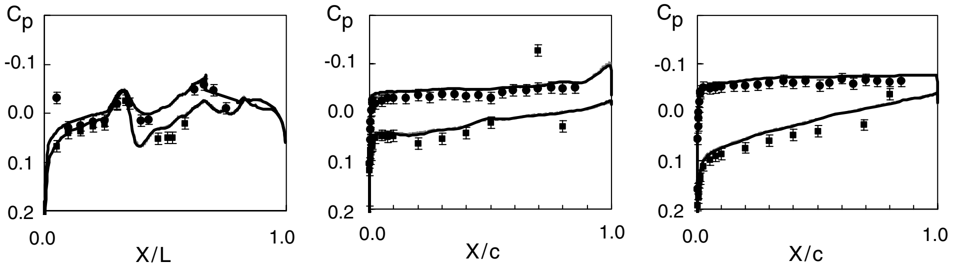

a) y/s=0.0 b) y/s=0.15 c) y/s=0.3

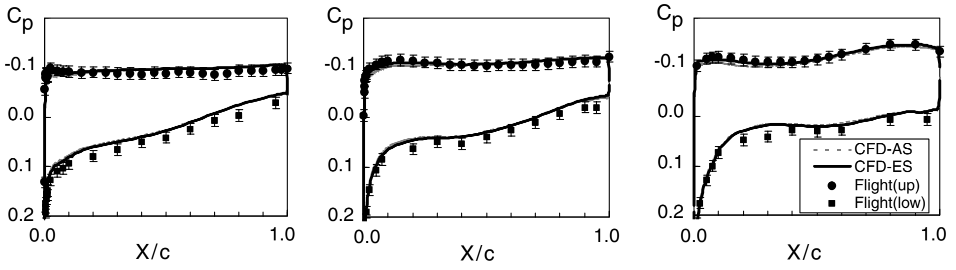

d) y/s=0.5 e) y/s=0.7 f) y/s=0.9

Fig. 16 C_p distribution at the design point (α-sweep no. 4, $\alpha = 1.59$ deg).

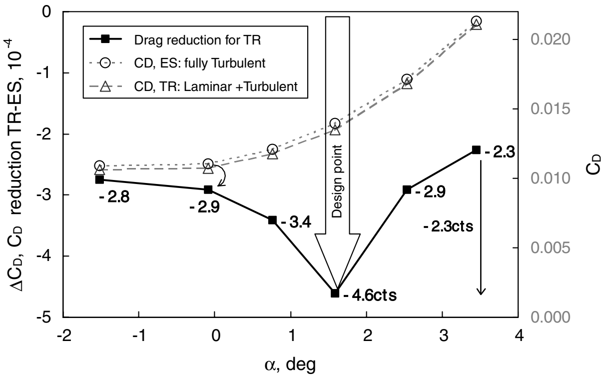

Fig. 17 Effect of natural laminar flow wing.

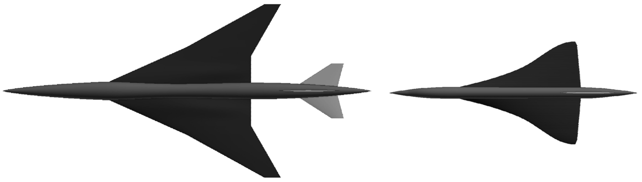

a) SST-A b) SST-B

Fig. 18 Configurations of the full scale SST.

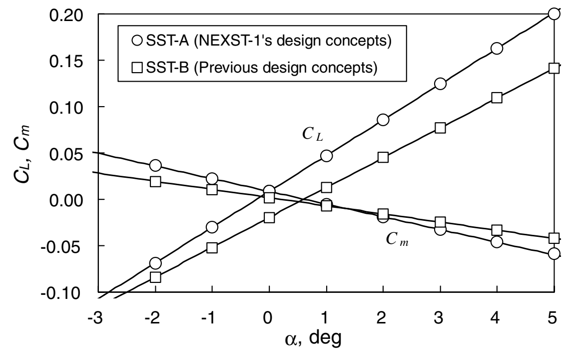

Fig. 19 C_L and C_M characteristics of SST-A and SST-B.

performance than the previous design concepts in the case of a full scale SST.

V. Conclusions

The CFD analysis of the NEXST-1 was performed to verify the aerodynamic design concepts for the drag reduction of the NEXST-1 using two CFD codes: structured mesh code UPACS and unstructured mesh code TAS. The validation of the CFD codes was performed in comparison with the wind-tunnel test. The CFD analysis was compared with the flight-test results. The effects of the aeroelastic deformation and the boundary layer transition data of the flight test were taken into account to improve the CFD analysis. And it was shown that the effect of the aeroelastic deformation improves the C_L, C_m, and C_p distributions, and the effect of the boundary layer transition improves C_D. The CFD analysis almost corresponds to the flight-test results. Some discrepancies were observed on both results; the reasons of the discrepancies are not clear, so further investigation is required. Finally, the effect of the natural laminar flow wing was assessed. It was found that the effect was the highest at the design point (α-sweep 4, $\alpha = 1.59$ deg), and the C_D was 4.6 counts smaller than that of the fully turbulent flow. It was confirmed that the concepts of the natural laminar flow wing design used by the NEXST-1 was effective during the flight test.

Finally, the real size SST using NEXST-1's design concepts was redesigned to clarify the benefit of the design concepts on the full

Table 3 The large scale SST

	SST-A	SST-B
Design concept	NEXST-1's design concept	Previous design concept such as Concorde
Planform	Arrow wing	Ogee wing
Warp	Carlson's optimum	Conical camber
Wing section	Natural laminar flow wing	NACA64A series
Fuselage	Area-ruled body	straight body
Passenger	300	100
Length, m	91.4	62

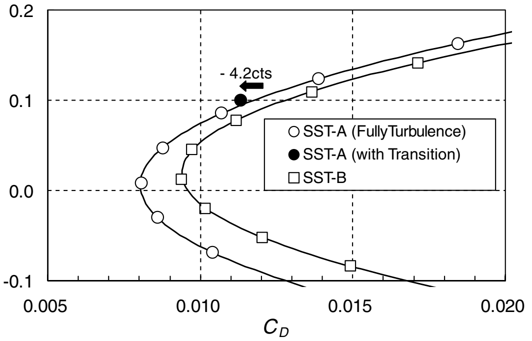

Fig. 20 Drag polar of SST-A and SST-B.

scale SST. For comparison, a previous type SST such as the Concorde was redesigned using previous design concepts and documents about the Concorde. We clarified that the design concepts of the NEXST-1 performed better than the previous design concepts in the case of a full scale SST.

Acknowledgments

The authors would like to acknowledge M. Murayama, Z. Lei, and F. Kuroda for their support of the CFD analysis, T. Takatoya and H. Kawakami for their structure analysis, and N. Tokugawa and Y. Ueda for their measurement and analysis about the boundary layer transition.

References

[1] Sakata, K., “Supersonic Experimental Airplane (NEXST-1) for Next Generation SST Technology—Development and Flight Test Plan for the Unmanned Scaled Supersonic Glider,” AIAA Paper 2002-0527, Jan. 2002.

[2] Ohnuki, T., Hirako, K., and Sakata, K., “National Experimental Supersonic Transport Project,” ICAS Paper 2006-1.4.1, Sept. 2006.

[3] Kwak, D., Yoshida, K., Ishikawa, K., and Noguchi, M., “Flight Test Measurements of Surface Pressure on Unmanned Scaled Supersonic Experimental Airplane,” AIAA Paper 2006-3483, 2006.

[4] Yoshida, K., and Makino, Y., “Aerodynamic Design of Unmanned and Scaled Supersonic Experimental Airplane in Japan,” *Proceeding of ECCOMAS 2004* [online database], http://www.mit.jyu.fi/eccomas2004/proceedings/proceed.html, Jyväskylä, Finland, July 2004 [retrieved 7 Jan. 2008].

[5] Kuchemann, D., *The Aerodynamic Design of Aircraft*, Pergamon, Oxford, England, U.K., June 1978.

[6] Carlson, H. W., and Miller, D. S., “Numerical Method for the Design and Analysis of Wings at Supersonic Speed,” NASA TN D-7713, 1974.

[7] Ashley, H., and Landahl, M., *Aerodynamics of Wings and Bodies*, Dover, New York, 1965.

[8] Jeong, S., Matsushima, K., Iwamiya, T., Obayashi, S., and Nakahashi, K., “Inverse Design Method for Wings of Supersonic Transport,” AIAA Paper 98-0602, Jan. 1998.

[9] Ishikawa, H., Kuroda, F., and Yoshida, K., “Study on Supersonic Drag Reduction Concept of SST—Comparison of Linear Theory and CFD Analsis,” *35th JAPAN Society for Aeronautical and Space Science Annual Conference*, Japan Society for Aeronautical and Space Sciences (JSASS), Yokohama, Japan, March 2004 (in Japanese).

[10] Takaki, R., Yamamoto, K., Ymane, T., Enomoto, S., and Mukai, J., “The Development of the UPACS CFD Environment,” *High Performance Computing, Proceedings of ISHPC 2003*, Springer, New York, 2003, pp. 307–319.

[11] Nakahashi, K., Togashi, F., Fujita, T., and Ito, Y., “Numerical Simulations on Separation of Scaled Supersonic Experimental Airplane from Rocket Booster at Supersonic Speed,” AIAA Paper 2002-2843, 2002.

[12] Spalart, P. R., and Allmaras, S. R., “A One-Equation Turbulence Model for Aerodynamic Flow,” AIAA Paper 92-0439, 1992.

[13] Kawakami, H., Takatoya, T., and Ishikawa, H., “Static Aeroelastic Analysis of Supersonic Experimental Airplane NEXST-1 Flight Test,” AIAA Paper 2007-4174, 2007.

[14] Tokugawa, N., Kwak, D. Y., and Yoshida, K., “Transition Measurements System Experimental Supersonic Transport NEXST-1,” ICAS Paper S2006-3.3.2, 2006.

[15] Tokugawa, N., and Yoshida, K., “Transition Detection on Supersonic Natural Laminar Flow Wing in the Flight,” AIAA Paper 2006-3165, 2006.

[16] Rech, J., and Leyman, C., *A Case Study by Aerospatiale and British Aerospace on the Concorde*, AIAA Professional Study Series, AIAA, New York, 1981.